A Novel Platform and Workflow for Underwater Photogrammetry Surveys

Alaa Mufti [1, 2, 3], Petra Helmholz [1], David Belton [1], Amir Allahvirdi-Zadeh [1] and Iain Parnum [1, 2]

[1] School of Earth and Planetary Sciences, Curtin University, Bentley, Western Australia
GPO Box U1987, Perth WA 6845, Australia, alaa.mufti@postgrad.curtin.edu.au, (P.Helmholz, D.Belton, Amir.Allahvirdizadeh, I.Parnum)@curtin.edu.au

[2] Centre for Marine Science and Technology, Curtin University, Bentley, Western Australia

[3] King Abdulaziz University, Rabigh 25732, Saudi Arabia

KEYWORDS: Underwater Photogrammetry, Calibration, GNSS PPK, Single Beam Echosounder.

ABSTRACT

Underwater photogrammetry has gained popularity for creating three-dimensional (3D) maps and ortho-images of marine environments as compared to traditional echosounder surveys, they can be more cost-effective at creating high-resolution 3D models, and orthoimages are usually more informative than acoustic backscatter maps. This paper builds on previous work by the authors that developed an underwater image-capturing platform with several additional sensors, including GNSS, IMU, pressure depth sensor and single beam echosounder. This study aims to analyse the impact of calibration and sensor data integration into the photogrammetric processing workflow. The tests were performed using two underwater sites. The low-cost device's pressure sensor and tide station data outperform GNSS PPK-derived heights. Furthermore, it was observed that incorporating IMU motion sensor data did not improve the processing results. Additionally, utilising the echosounder point cloud proves valuable for enhancing the overall quality of the survey. Despite its lower density, it serves a dual purpose by validating the photogrammetry dataset and, more importantly, can be employed for correcting DSM height. This study further underlined the importance of reliable camera calibration for accurate 3D reconstruction.

1. Introduction

Accurate maps of bathymetry and seafloor habitat, allow for the prediction and mitigation of various environmental impacts (Pickrill and Todd, 2003). Thus, the evolution of underwater mapping and monitoring technology enhances our potential understanding of the sea and coastal areas, benefiting management efforts. Mapping the marine environment has traditionally been carried out via aerial and satellite remote sensing or vessel-based echosounder surveys (Parnum et al., 2009; Brown et al., 2011). More recently, underwater photogrammetry has gained popularity for creating three-dimensional (3D) maps and ortho-images of marine environments (Nocerino et al., 2020). It can be carried out by scuba divers and remotely operated or autonomous underwater vehicles (Mahrad et al., 2020, Rofallski et al., 2020). However, achieving high accuracy in the geolocation and scale of underwater models generated from photogrammetry can be more challenging than terrestrial environments. This is because calibration and positioning methods are more difficult for underwater surveys, which can mean the interior and/or exterior orientation parameters are not adequately calculated. Additional sensor data must be integrated with the images, offering a georeferenced location and a point cloud (Rofallski et al., 2020).

This paper builds on previous work by the authors that developed an underwater image-capturing platform that uses open-source devices to log the position and motion of the rigid camera frame using several sensors installed on the platform (Mufti et al., 2023a). The platform is designed to conduct underwater photogrammetry surveys. The motivation of this study is to use the advantages of traditional single-beam echosounder surveys and contemporary underwater photogrammetry methods, effectively addressing the inherent limitations of each approach. Specifically, the aim is to leverage the precise GNSS positioning and reliable bathymetric data acquired through single-beam surveys. This information is used as a robust reference framework for enhancing the accuracy of the photogrammetry workflow. The synergy between these methodologies is designed to overcome the constraints associated with standalone single-beam surveys and photogrammetry techniques. By combining these traditional and contemporary survey methods, the study offers a novel approach that not only mitigates their individual limitations but also unlocks new possibilities in underwater mapping and visualization.

This study aims to analyse the impact of calibration and sensor data integration into the photogrammetric processing workflow. In other words, additional information captured by the imaging platform is used to constrain the image processing pipeline. The study area of this paper is an area with artificial reef structures close to the shoreline. The resulting 3D models of these artificial reefs are compared to bathymetric multibeam survey data of the area and an aerial ortho-image of the structures to evaluate the performance of the calibration frame and the positioning methods.

The paper is structured as follows: In section 2, we will briefly review the platform introduced in Mufti et al. (2023a) and the study area. Next, in section 3, we will introduce the method for processing the sensor and image data captured from an underwater photogrammetry survey of the artificial reef. In section 4, we validate outputs. The paper concludes with a conclusion and outlook in section 5.

2. Platform and study area

Mufti et al. (2023a) introduced a platform (Figure 1) to collect ancillary data for underwater photogrammetry surveys. The platform carries the sensors as presented in Table 1. It uses a Raspberry Pi to collect time-synchronised data, including (X, Y, Z) position, depth, altitude and motion.

In this study, three GoPro 5 cameras were mounted to the platform’s rigid frame, positioned underwater just below the surface (Figure 1). These GoPro 5 cameras were used as they have been shown to perform well when used for underwater photogrammetry (Helmholz et al., 2016).

The platform with mounted cameras was used to conduct an underwater photogrammetry survey of sublittoral artificial reefs in Coogee Beach, near Omeo Wreck, West Australia (WA)

(-32.105189° E, 115.761165° S) on the 26th of August 2023. Two study areas (1 and 2) were chosen for analysis and are shown as white polygons in Figure 2. Figure 2 also shows part of the platform track. The ortho-image and multibeam bathymetry captured in 2021 by the WA Government are shown in Figure 2 (at 10 cm grid size). The multibeam bathymetry was the closest in time to our survey in 2023, and the ortho-image had the best visibility in recent aerial surveys.

	Type	Product	Measuring of
1	GNSS	SparkFun GPS-RTK Board – NEO-M8P-2 Receiver	Location and altitude
2	Pressure sensor	BlueRobotics Bar30 High-Resolution 300m Depth/Pressure Sensor	Depth
3	IMU	Raspberry Pi Sense HAT V2	Motion
4	Single-beam echosounder	BlueRobotics Ping Sonar Altimeter and Echosounder	Sparse point cloud
5	Cameras	GoPro Hero 5 (set to 4000 x 3000 pixels, f/2.8, 1/330 sec exposure and ISO-100)	Images

Table 1. Overview of sensors on data capture platform.

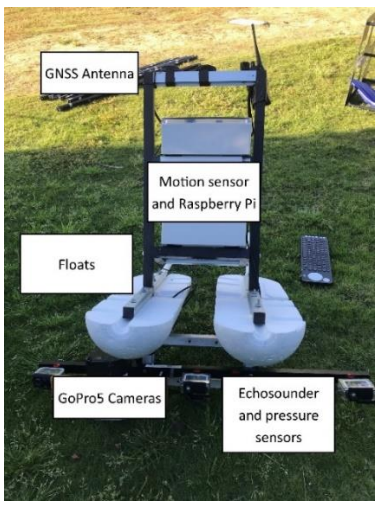

Figure 1. Platform used to carry out underwater photogrammetry and echosounder surveys.

3. Methods

In this section, we will introduce the processing of the sensor data, followed by a description of the image processing pipeline. The aim is to apply a standard photogrammetric processing pipeline but to constrain the adjustment by utilising the sensors that are part of the capturing platform.

3.1 Sensor data processing

3.1.1 GNSS processing

The platform has a built-in Global Navigation Satellite System (GNSS) receiver that can be used to obtain the platform's location when images are captured. The location information can be used to constrain the image processing pipeline. Mufti et al. (2023a) concluded that GNSS post-processing kinematic (PPK) provides the best position information available for the image processing pipeline. Hence, this method is applied here.

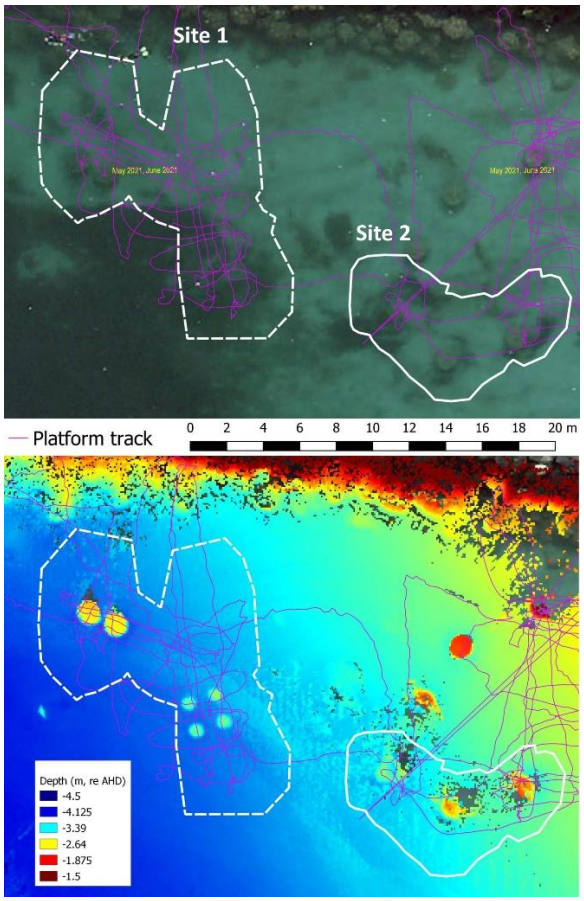

Figure 2. Platform tracks of the underwater photogrammetry survey (in magenta) over an aerial photo (top) and multibeam bathymetry (bottom). The two white polygons show the location of study areas 1 (dashed line) and 2 (solid).

As there were no existing survey marks near the survey area, a base station was established < 100 m from the survey area, using a Trimble R12 receiver logging for three and half hours in static mode. The base station was used to log data to enable PPK to be carried out. The data collected at the base station was processed using a long-baseline approach using the Australian Online GPS Processing Service (AUSPOS) developed by GeoScience Australia (https://gnss.ga.gov.au/auspos). The 95% positioning uncertainty of the base stations following AUSPOS processing was 0.014 m (X-Y) and 0.167 m (Z). Analysis of the X-Y positioning data showed a difference of 10-30 cm in absolute position (accuracy) in places, which was consistent with Mufti et al. (2023a). The raw GNSS code and phase observations from the platform were processed with the adjusted base station data, using RTKLIB to carry out PPK (Takasu, 2013). Data were exported in Map Grid of Australia (MGA50) and heights re Australian Height Datum (AHD).

3.1.2 Pressure sensor measurements

As an alternative method of estimating the elevation of the platform, it is possible to use the pressure sensor installed on the platform. The pressure data was converted to a depth using the standard UNESCO endorsed formula, and then corrected for tide using measurements from the WA Government tide station at Fremantle Fishing Boat Harbour 6 km away. As the tide measurements were relative to chart datum (CD), an offset of 0.756 m was applied to transfer these values to AHD.

3.1.3 Motion data

Other measurements that can constrain the photogrammetric workflow are the motion information captured by the inertial measurement unit (IMU) installed onto the imaging capturing platform. A series of simple calibration exercises were carried out to calculate values of roll, pitch, and yaw relative to the frame and in the convention used in the photogrammetry workflow. The yaw was also corrected for magnetic declination, as the heading sensor was a magnetic compass.

3.1.4 Single-beam echosounder depths

The single-beam echosounder data collected by the platform during the survey was time-tagged with the PPK position data and corrected for sound velocity and physical offsets. The seafloor depth was calculated in two ways: 1) by reducing the soundings with the pressure sensor data and tide observations as per Mufti et al. (2023a), and 2) by using the PPK heights. Both were exported as a point cloud referenced re AHD. The derived sparse point cloud was investigated to add constraints to the image processing pipeline and as a correction post-photogrammetry workflow.

3.2 Image processing

3.2.1 Photogrammetric workflow

Photogrammetric 3D reconstructions were carried out using Bentley’s Context Capture (CC) software (v10.19.0.122). The processing pipeline followed a classical photogrammetric processing workflow, including the initial alignment of all images based on automatically extracted feature points, the inclusion of control as per the processed dataset, a least squares bundle block adjustment, followed by the creation of dense point clouds, meshes and ortho-images (ortho-images). The least squares adjustment was constrained by the different inputs of the other sensors. An overview of the different constraints is provided in Table 2. For instance, the least squares adjustment can be performed using an X, Y, and Z constraint on the platform's location based on the GNSS PPK results. However, the Z component can also be used from the pressure sensor corrected for tide. All Z values are in the AHD to make the results comparable.

	Sensor data used	Constraint applied
1	GNSS PPK	X, Y, Z
2	Pressure sensor (+ tide)	Alternative solution Z
3	IMU	Pitch, Roll, Yaw
4	Single-beam echosounder	Dense Point Cloud

Table 2. Constraints to the bundle adjustment.

A Digital Terrain Model (DTM) was also created from the Digital Surface Model (DSM), by manually removing the artificial reefs from the data in CloudCompare (2.12 beta). Finally, ortho-images were created using CC. All relevant parameters are presented in Table 3.

	Process	Parameters
1	Dense Image matching	Resolution: 0.0011 m Projection mode: Highest point
2	Ortho-image	Ground Sample Distance: 0.01 m

Table 3. Utilised parameters for the image processing.

3.2.2 Camera calibration

In addition, three different methods of camera calibration are applied to the images. Next to the self-calibration based on the images captured (selfCal) two calibration frames are utilised. The two frames were introduced in Mufti et al. (2023b) - rigid cube (Figure 3, left), and a collapsible pyramid (Figure 3, right). Both were submerged near the test area, and several images were taken while collecting the main data. The camera is calibrated based on those images, and the camera calibration parameters are applied when the images of the test sites are processed. An overview of the calibration methods is provided in Table 4.

	Calibration	Explanation
1	selfCal	Self-calibration based on the images captured of the test sites
2	calC	Calibration using cube frame
3	calP	Calibration using collapsible pyramid

Table 4. Calibration methods allied during image processing.

The camera calibration parameters that are solved are focal length (*c*), principal point offset (*XP*, *YP*), radial lens distortion parameters (*k1-k3*), and decentring distortion parameters (*p1*, *p2*). The camera calibration parameters are calculated during the pre-calibration and then applied during further processing.

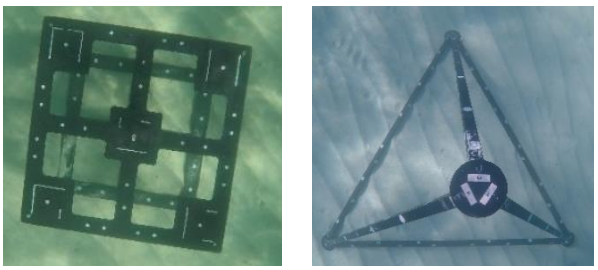

Figure 3. Calibration frame for the pre-calibration of the camera. Cube (left) and collapsible pyramid (right).

4. Evaluation

For the evaluation, a multibeam bathymetry dataset was available. The multibeam bathymetry was captured in 2021 by the WA Government. This is a challenge as the site has changed between 2021 and 2023. For instance, additional structures were submerged, and the ocean seafloor (sand) has changed. However, due to the lack of any other reference data, we had to utilise this slightly outdated dataset.

When point clouds are compared, a point-to-surface comparison between the different clouds is performed, whereas the surface is defined by the 8 nearest neighbour points. No alignments of the point clouds were performed for geo-referenced datasets. The resulting distances are shown in histograms through which a Weibull distribution is fitted. The metrics used to quantify the differences between the point clouds are provided in Table 5. For the comparisons, CloudCompare was utilised.

4.1 Camera calibration

4.1.1 Comparison of results using the two different fames

Firstly, we want to establish if there are significant differences when applying the calC and calP methods. The results of calibrating the three GoPro 5 cameras using these two methods are summarised in Table 6. The GNSS location and pressure and tide information for depth were also utilised for both datasets. Using the calP for the calibration, produced results with a reprojection error (RMS) of 2.05 pixels and the RMS of distances to rays of 3.6 mm. The calC performed better, with a reprojection error (RMS) of 1.4 pixels, and a RMS of distances to rays of 2.9 mm.

The calP structure did not perform as well as it did in Mufti et al. (2023b). A possible reason is the geometry in which the images were captured. Figure 4 shows clearly that the camera stations

during the capture of calP are closer to each other, consequently leading to not justifying calibration results. This highlights the significance of careful selection of the configuration camera stations during the data capture.

Parameter	Explanation
Weibull shape parameter *a*	A large *a* means the distribution is moved away from zero, so significant distances are present between the compared point clouds.
Weibull scale parameter *b*	0 < *b* < 1, the larger the number, the distribution is more stretched out.
95% confidence interval [m]	It determined the distance in which 95% of the calculated distances fall.
Mean, Mode [m]	The Mean and Mode of the point cloud distances.
Shift (X, Y, and Z) [m], Scale	If the locations of two different point clouds are compared, their shift vector and their different scales are compared.
STD, RMS [m]	Standard deviation (STD) between the mean and samples as well as Root Mean Squared (RMS) of the alignment.

Table 5. Parameters used in the comparison of point clouds.

Camera	RE	D2R	#images	F	XP	YP
calC						
Left	1.4	2.9	128/175	20.94	1998	1493
Mid	1.4	2.9	97/144	20.8	1992	1493
Right	1.4	2.9	146/232	20.78	2028	1481
calP						
Left	2.05	3.6	39/42	21.16	1993	1491
Mid	2.05	3.6	16/26	21.61	2095	1582
Right	2.05	3.6	81/83	21.19	2037	1490

Table 6. Parameters from the pre-calibration of three cameras (Left, Mid and Right) using the Cube and Pyramid frames. The focal length (F) is provided as Equivalent 35 mm. XP and YP are the principal point offsets in X and Y provided in pixels. D2R = Distance to rays (mm). RE = Reproj. (RMS) pixels.

The impact of the not optimal camera station layout during the data capture for calP is likely to be the source for the quite different camera calibration parameters (Table 6). For instance, the focal length of calC is constantly shorter than using calP for all three cameras used (Table 6).

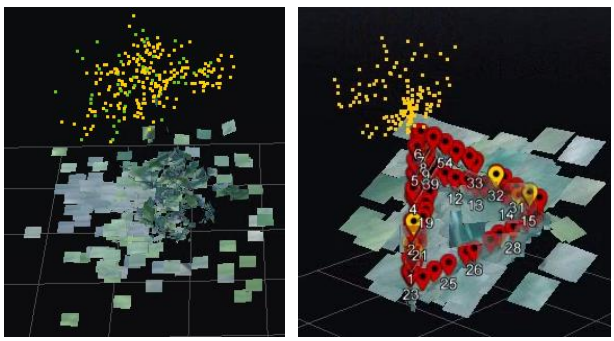

Figure 4. Distribution of camera stations compared to the calibration frame (Left: calC, Right: calP).

4.1.2 Self-Calibration (selfCal) with and without additional sensor information

In contrast to the pre-calibration using the calC or calP method, it is also possible to perform a self-calibration based on the images captured from the test sites. Self-calibration is known to create a bowing or doming effect if the data capture is not performed in a geometry suitable for self-calibration, e.g. using orbital “flights” with high overlap. While it is possible to perform well-considered and easy-to-execute flight planning for in-air applications (e.g. for drones), this is not always the case underwater.

The outcomes of the self-calibration performed for test site 2 are detailed in Table 7. For this test, only the results of site 2 are presented, and are comparable to the results of test site 1. Using the test site 2 dataset, two different tests are performed. Firstly, a self-calibration is performed without additional constraints such as Sensor Data (SD) (selfCal-NoSD). This means no GNSS and depth sensor data is used. The second self-calibration uses the GNSS location data and additional pressure and tide data for depth measurements (selfCal-WithSD). The utilisation of additional sensor information is hoped to enhance the calibration's robustness and reliability, contributing to more accurate and meaningful results in the subsequent analysis. However, Table 7 does not show any indicators for a more reliable calibration when adding the sensor data (GNSS X, Y), pressure sensor and tide (Z). The reprojection errors are similar, and the focal length as well as *XP* and *YP*, are comparable. The results are even comparable with the calibration results achieved by calC and calP in Table 6. The only difference is a slightly different focal length.

Camera	RE	D2R	#images	F	XP	YP
self-Cal with no additional Sensor data (NoSD)						
Left	1.3	0.06	239/ 244	21.27	2019	1486
Mid	1.3	0.06	246/ 252	21.3	2006	1488
Right	1.3	0.06	248/ 253	21.33	2022	1487
self-Cal with additional Sensor data (WithSD)						
Left	1.4	0.02	177/ 178	21.24	2007	1492
Mid	1.4	0.02	179/ 188	21.3	1996	1497
Right	1.4	0.02	170/ 170	21.33	2014	1497

Table 7. SelfCal parameters with no and with additional sensor data for the three cameras (Left, Mid and Right) calculated based on test site 2. The focal length (F) is provided as Equivalent 35 mm. XP and YP are the principal point offsets in pixels. D2R = Distance to rays (mm). RE = Reproj. (RMS) pixels.

4.1.3 Pre-calibration vs self-calibration

Next, we compare the estimated parameters for pre- and self-calibration. A special focus is given to the radial lens distortion, as those are correlated with the appearance of the bowing/doming effect. The radial lens distortion profiles for calP, calC, selfCalWithSD and selfCalNoSD of the right camera are shown for site 1 Figure 5. The largest correction values are always present for the CalP method (blue profile). The CalC method (grey profile) is “in-between” the CalP and the selfCal methods. The selfCal methods with (selfCalWithSD, yellow profile) and without (selfCalNoSD, orange profile) sensor data have very similar profiles. The left camera produces a very similar radial

lens distortion plot (not shown). However, the centre camera shows a stronger alignment of the selfCal methods with (selfCalWithSD) and without (selfCalNoSD) sensor data for both site profiles to CalC (not shown). This could be explained by the different viewing angles of the centre camera compared to the right and left cameras.

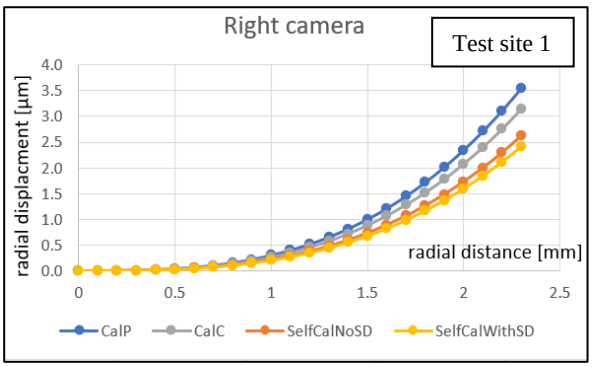

Figure 5. Radial lens distortion profiles of the right camera using the different calibration methods, test site 1.

4.2 Sensor data impact on DTM and DSM products

Further investigations regarding the impact of the calibration parameters on the derived DTM/DSM are presented in the next section.

4.2.1 Impact of different camera height information

Due to the sensors installed on the platform, the depth of the cameras (i.e. their elevation re AHD) information can be derived using two methods. One was using the elevation data from the GNSS PPK, and the other using the pressure and tide station data. The impact of the different depth inputs was quantified using the DTMs produced using these methods, compared with the reference multibeam data. Due to the low quality of the multibeam data from the shallower site 2, only site 1 was compared. As site 2 changes between when the multibeam data was captured to our data collection (new artificial reefs were added), we are comparing the DTM and not the DSM.

The site 1 DTM produced using the constraint of the pressure & tide data was closer to the reference surface, than the DTM produced using the PPK elevation, both visually (Figure 6) and in performance metrics (Table 8). For instance, the mean difference between the multibeam surface and the DTM produced using the pressure & tide data was 6 cm, compared to 27 cm for the DTM produced using the PPK height (Table 8).

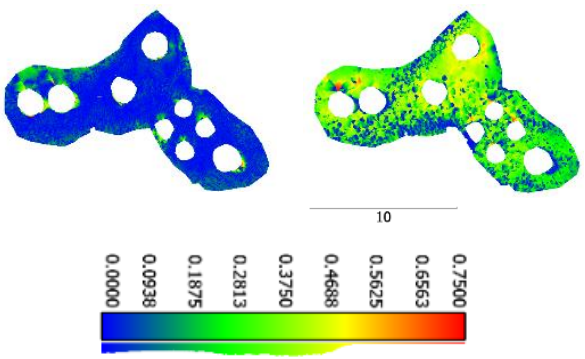

Figure 6. Comparing DTMs for site 1 produced using pressure sensor and tide data (dataset 4, left), and PPK height (dataset 2, right) vs multibeam. In meters.

Dataset	95% [m]	a	b	Mode [m]	Mean [m]	STD [m]
PPK height	0.48	1.71	0.29	0.37	0.27	0.14
Pressure & tide	0.21	0.95	0.06	0.0	0.06	0.08

Table 8. Comparison results of the DTM derived from PPK height and pressure and tide vs multibeam for test site 1.

4.2.2 Impact of the combination of calibration method and different depth information on the DSM

Previously, we established that the calibration method and the depth information can impact the results of the reconstruction significantly. The best results have been achieved using calC and GNSS positioning outputs (X,Y) with pressure and tide for elevation (Z). We have also established that adding sensor information has little impact on the selfCal result of the camera calibration parameters. While the camera calibration parameters (besides the radial lens distortion profiles) are very similar, we now try to establish if adding location and depth data into the processing has an impact on the resulting DSM. For the analysis, we utilise the test site 2 results. The reference used was the dataset processed with the best-performing methods so far (calC, GNSS positioning outputs (X,Y), pressure and tide for elevation (Z)).

We are going to compare the reference dataset to the following:

1. Dataset 1: self-cal with pressure sensor and tide
2. Dataset 2: self-cal with PPK Height
3. Dataset 3: Pre-Calibrated (Cube) with PPK height

The results of the comparison are shown in Table 9. In comparing these scenarios against the reference dataset, dataset 3 demonstrates superior performance, with a significantly smaller 95% confidence interval (0.09 m vs 0.57 m and 0.16 m). The RMS error is also significantly lower (0.083 m vs 0.187 m and 0.192m). However, it must also be highlighted that introducing additional location and depth information into the self-calibration improves the results.

Remarkable is the shift in z-direction (Table 9), which for the self-calibration datasets (-0.076 m and -0.481 m) is very different from the pre-calibrated dataset (0.228 m). Firstly, the sign is the opposite, and secondly, the magnitude is much larger. It is known that any calibration error impacts the depth estimation, which can be seen to be clearly the case here.

The results suggest that DSMs produced using pre-calibration (and camera height), are more accurate and precise data than self-calibration (with camera height data), making it the preferred method. The effectiveness of pre-calibration is evident in the smaller deviations from the reference, highlighting its potential for enhancing the accuracy and reliability of positioning data in underwater photogrammetry applications.

Comparing the DSM point clouds of dataset 1 to dataset 3 to the reference (Figure 7) clearly shows the strong bowing of the selfCal datasets (1 and 2). For this comparison, the shift presented in Table 9 has been eliminated, but the scale has not been adopted. The bowing effect is mostly in the north/south direction. For dataset 2, the bowing is also in the east/west direction. The area indicated by the black arrow in Figure 7 exceeded the defined limit of 0.6m and is, for this reason, not presented. In contrast, dataset 3 shows only a small bowing effect, again in the north-south direction, but in the opposite direction of datasets 1 and 2. The resulting bowing/doming effect due to incorrect radial

lens distortion parameters, is in line with the results of other researchers (Carbonneau & Dietrich, 2017; Habib et al., 2005).

	1. Self- cal., pressure & tide	2. Self- cal., PPK Height	3. CalC., PPK height
95% [m]	0.57	0.16	0.09
a	1.0381	0.986	0.9728
b	0.1891	0.175	0.0261
Mode [m]	0.002	0.002	0.005
Mean [m]	0.186	0.176	0.026
STD [m]	0.179	0.189	0.029
Shift x [m]	-0.067	-0.086	0.065
Shift y [m]	0.099	0.048	0.050
Shift z [m]	-0.076	-0.481	0.228
Scale [m]	1.036	1.030	1.002
RMS [m]	0.187	0.192	0.083

Table 9. Comparison results of the DSM derived from different combinations of calibration and depth information.

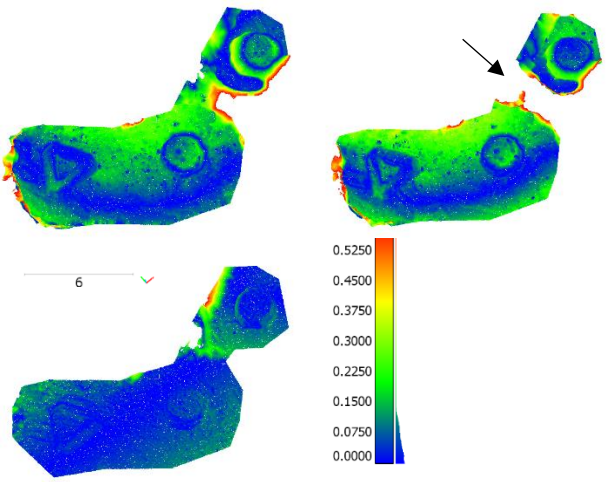

Figure 7. DSM of the reference dataset with dataset 1 (top right), dataset 2 (top left) and dataset 3 (bottom).

4.2.3 Impact of Motion Data

To assess the impact of motion data on the calibration process, two scenarios were compared: self-calibrated with pressure sensor and tide with motion and self-calibrated PPK height with motion. The reference dataset is the same as in the previous test (in 4.2.2), so cube pre-calibration and using pressure and tide for elevation. The results are presented in Table 10. Again, the results using pre-calibration outperform the dataset with self-calibration. The 95% confidence interval is less than half (0.164m vs 0.096m). However, the difference is not as much as the previous test, e.g. only 1.2 cm between their mean differences with the reference surface. Interestingly, the RMS values for the self-calibration improved when adding motion information (Table 9: 0.187m vs 0.143m in this test), but the RMS increases for the pre-calibrated dataset: 0.083m vs 0.193m in this test (Table 9 and Table 10).

A possible reason for the motion information to decrease the accuracy is the environment. The sensor is surrounded by metal and other sensors that could potentially interfere with data collection and the presence of small waves and pumps in the models was attributed to the waves on the seafloor. A more rigorous calibration of the IMU, or the use of an array of GNSS antennae, is expected to improve the results but is outside of the scope of this paper.

	Self- cal., pressure & tide with motion	Pre-Cal PPK height with motion
95% [m]	0.164	0.096
a	0.8331	1.1350
b	0.0427	0.0351
Mode [m]	0.001	0.008
Mean [m]	0.047	0.035
STD [m]	0.063	0.031
Shift x [m]	0.053	-0.019
Shift y [m]	0.035	0.077
Shift z [m]	-0.024	0.203
Scale [m]	1.029	0.989
RMS [m]	0.143	0.193

Table 10. Comparison results of the DSM derived from different combinations of depth information together with added motion information.

4.3 Impact of single-beam depth data

The single-beam depth data can be used to create a sparse point cloud, which can also be used to constrain the least squares adjustment, and outside of the photogrammetry workflow to validate and/or adjust the 3D models.

4.3.1 Validation of single-beam depth data using multibeam data

As the first step, we analyse the quality of the Single-beam depth data by comparing the data to the multibeam dataset, using both vertical reduction methods. The data agreed well with the historic multibeam bathymetry (Figure 8). The correlation was slightly higher (R = 0.88) and RMS slightly lower (0.33 m) for the soundings reduced using tide, compared to using the PPK Height (R = 0.86, RMS = 0.34 m).

4.3.2 Comparison of elevation vs echo-sounder altitude for camera heights

The use of the single beam data was investigated as a way to position the camera’s height as an altitude (as opposed to the previously used elevation) in the photogrammetry workflow. The DSM generated from this approach was compared with the, so far, best-performing dataset processed using CalC, GNSS location outputs (X,Y), and pressure & tide depth data (Z, i.e. elevation) without motion information. The provided numerical breakdown (Table 11), shows that the camera height is better referenced as an elevation than altitude in the workflow, with a 95% confidence interval ranging from 1.7 to 2.5 m. The mean value of 2.56 m and the standard deviation of 0.40 m (Table 11), illustrate the exterior orientation parameters determined by the photogrammetry workflow are better when it derives the altitude, rather than images being tagged with it.

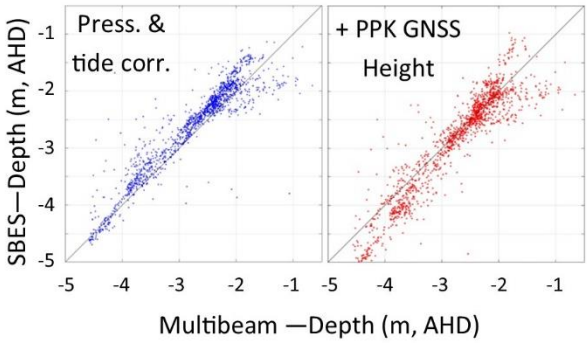

Figure 8. Single beam echosounder (SBES) depth values from this survey compared to historic multibeam depths collected in 2021: Left: soundings reduced using the pressure and tide, Right: soundings referenced using the PPK height.

	95% [m]	a	b	Mode [m]	Mean [m]	STD [m]
SBES	2.73	8.52	2.5	2.6	2.4	0.40

Table 11. Comparison of single-beam echo-sounder (SBES) depth data vs photogrammetry

4.3.3 Integrating the single-beam beam data into the photogrammetry workflow

The integration of the single beam depth data into the photogrammetry workflow was investigated. However, CC software omitted the single beam point cloud in the workflow, citing its lower density. This led to an additional layer beneath the photogrammetry point cloud, as shown in Figure 9. The exclusion of the single beam data indicates the software's preference for higher-density datasets, which aim to bolster the fidelity and detail of the resulting reconstructions by strategically leveraging photogrammetric and echosounder datasets.

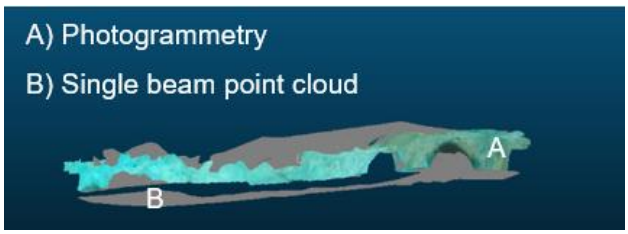

Figure 9. Fusion of echosounder data with photogrammetry.

4.3.4 Validation of using single beam data to correct DSMs that used GNSS heights

We evaluated whether the single-beam echosounder (SBES) depths can improve the accuracy of the DSM, post-photogrammetry workflow. In previous tests, the PPK height information achieved constantly worse results compared to the datasets processed with pressure and tide. In this test, the DSM derived using PPK heights is corrected using the SBES depth data. Hence, the following datasets are processed and then compared to the multibeam reference dataset:

- dataset 1: CalC, GNSS (X, Y, Z), no motion data
- dataset 2: CalC, GNSS (X, Y), pressure & tide (Z), no motion data
- dataset 3: Same as Dataset 1, then the resulting DSM has its Z value corrected using linear regression against the SBES.

The results are presented in Table 12, show that Dataset 1, representing PPK height, had a higher mean difference with the reference surface (24.8 cm) compared to dataset 2, which represents pressure and tide (14.7 cm). However, a corrected PPK height using linear regression with the SBES depth data (dataset 3), had a mean difference of 17.4 m. This represents a notable improvement over dataset 1, reducing the mean error by 30%. The effectiveness of the SBES correction applied post the photogrammetry workflow, can be further seen by visually comparing the multibeam depth (Figure 10a) with the DSMs of datasets 1 (Figure 10b) and 3 (Figure 10c), and SBES depths (Figure 10d).

	dataset 1	**dataset 2**	**dataset 3**
95% CI [m]	0.491	0.590	0.597
a	1.465	0.797	0.948
b	0.271	0.128	0.170
Mode [m]	0.015	0.016	0.002
Mean [m]	0.248	0.147	0.174
STD [m]	0.155	0.195	0.192

Table 12. Comparison results of the DSM derived from different combinations with multibeam reference dataset.

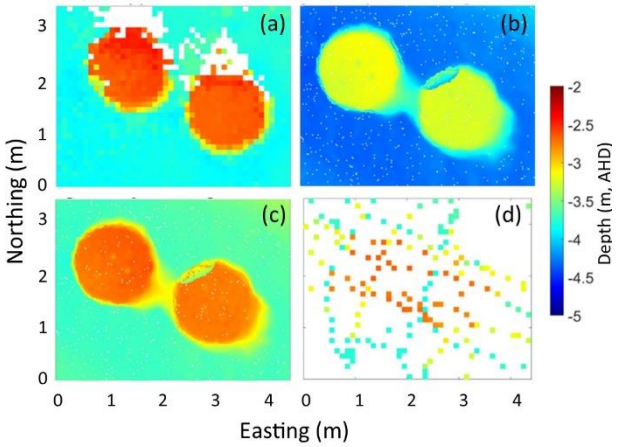

Figure 10. (a) multibeam data. B) photogrammetry with incorrect depths. C) photogrammetry – with SBES correction. D) SBES depth.

4.4 Photo mosaics

Photo mosaics generated using the combination of cube calibration and pressure sensor and tide for camera height (as well as PPK for camera X-Y positioning), for site 1 and site 2 are shown in Figure 11. Compared to the multibeam and aerial ortho-image captured in 2021 (Figure 2), two of the round “Bomboras” in site 1 are not present, as it appears they have not been deployed, yet. The difference between the location of the reef structures in multibeam and aerial captured ortho-image in (Figure 2), and the photo mosaics in Figure 11 is < 30cm. This was without any GCPs. Additionally, in the aerial-captured ortho-image, it is hard to make out the group of four “Apollo” (Figure 2), compared to the ortho-image produced in this study (Figure 11). This is due to a combination of the water surface impeding the aerial image capture, and the higher resolution of this study due to the cameras being closer to the survey area. This highlights the advantage of capturing images underwater compared to an above-water aerial platform. In addition, Site 2 is quite shallow (< 3 m), as a result, the multibeam data is sparser and noisier (than site 1), meaning the structures are less defined than the photogrammetry DSMs. This highlights an advantage of using photogrammetry over multibeam echosounders in very shallow water.

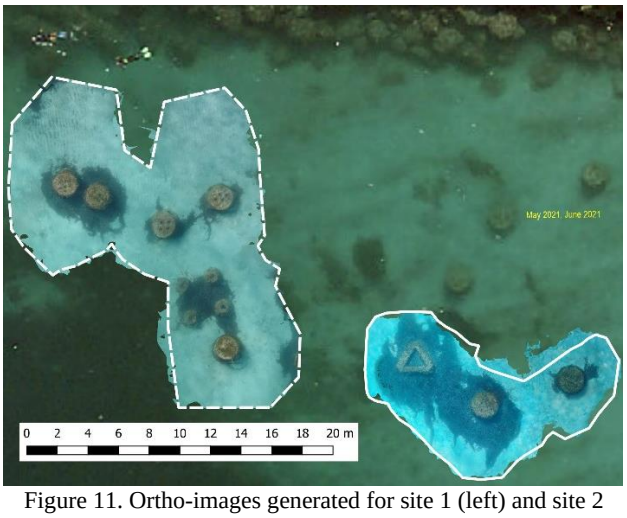

Figure 11. Ortho-images generated for site 1 (left) and site 2 (right) over an aerial photo.

5. Conclusion and Further work

The challenges of underwater photogrammetry surveys, particularly in achieving accurate calibration and precise positioning, can often lead to inaccuracies in determining interior and exterior orientation parameters. This study addresses these challenges by building upon prior research by the authors. The survey platform (Mufti et al, 2023a) and camera calibration frame (Mufti et al, 2023b) previously developed, were employed in an underwater photogrammetry survey on an area featuring artificial reef structures. The 3D models generated from this survey were validated using bathymetric multibeam survey data. This comparison aimed to assess the effectiveness of using a calibration frame and the positioning methods, specifically evaluating their impact on the accuracy of geolocation and scaling in the context of underwater photogrammetry.

Carrying out a pre-calibration using a dedicated 3D structure, produced more accurate 3D models than the self-calibration method. This is consistent with other studies (Shortis, 2019). Of the two calibration frames tested, the rigid cube outperformed the collapsable pyramid. Reasons for this might be the geometry in which the images were captured, or the collapsable frame might not be consistently rigid.

The impact of the sensor data derived from the platform on the photogrammetric processing was analysed. Among these, the pressure sensor measurements combined with and tide station, emerged as more effective in accurately tagging the camera height than GNSS PPK height.

It was observed that incorporating the motion sensor data did not improve the processing results. However, the calibration of the sensor and the use of high-grade IMUs, especially using a secondary GNSS antenna, should be considered in future studies.

Although the single beam depth point cloud could not be incorporated in the photogrammetry workflow, due to its relatively low density, proved valuable for enhancing the overall quality of the survey. Despite its lower density, it can serve the dual purpose of validating DSM heights, and where necessary, correcting the heights of DSMs.

We concluded an optimal workflow for this study was to: carry out a dedicated, in-situ pre-calibration using a rigid 3D structure; tag images with GNSS PPK X-Y positions; use pressure sensor and tide station measurements for the camera height; and collect echosounder data to enable validation and as a fail-safe for correcting any erroneous heights. Using this approach produced a DTM that had an RMS of 6 cm compared to multibeam, and a geolocation error of < 30cm. This was done without the use of GCPs, which are challenging to create in an underwater setting. This study, thus, has presented the notable benefits of pre-calibration of cameras using a 3D structure, and the integration of single-beam bathymetry into the photogrammetry workflow.

Acknowledgements

The authors would like to thank King Abdulaziz University for funding Alaa Mufti’s PhD study, and Mr Malcolm Perry and Mr Ming Lim from Curtin University for technical support. We also thank Curtin’s 3D Hub for the opportunity for the data processing.

References

Brown, C. J., Smith, S. J., Lawton, P., & Anderson, J. T. 2011. Benthic habitat mapping: A review of progress towards improved understanding of the spatial ecology of the seafloor using acoustic techniques. Estuarine, *Coastal and Shelf Science*, 92(3), 502-520.

Carbonneau, P. E., & Dietrich, J. T. 2017. Cost-effective non-metric photogrammetry from consumer-grade sUAS: implications for direct georeferencing of structure from motion photogrammetry. *Earth Surface Processes and Landforms*, 42(3), 473-486.

Habib, A., Ghanma, M., Morgan, M., & Al-Ruzouq, R. 2005. Photogrammetric and LiDAR data registration using linear features. P*hotogrammetric Engineering & Remote Sensing*, 71(6), 699-707.

Helmholz, P., Long, J., Munsie, T., & Belton, D. 2016. Accuracy assessment of go pro hero 3 (Black) camera in underwater environment. *The International Archives of the Photogrammetry, Remote Sensing and Spatial Information Sciences,* 41, 477-483.

Mahrad, B. E., Newton, A., Icely, J. D., Kacimi, I., Abalansa, S., & Snoussi, M. 2020. Contribution of remote sensing technologies to a holistic coastal and marine environmental management framework: a review. *Remote Sensing*, 12(14), 2313.

Mufti, A., Parnum, I., Belton, D., & Helmholz, P. 2023a. An open-source, data-logging device for marine-based surveys. I*nternational Archives of the Photogrammetry, Remote Sensing & Spatial Information Sciences*, II WG II/7.

Mufti, A., Parnum, I., Belton, D., & Helmholz, P. 2023b. introduction and validation of a novel calibration frame. I*nternational Archives of the Photogrammetry, Remote Sensing & Spatial Information Science*s, II WG II/7.

Parnum, I., Siwabessy, J., Gavrilov, A., & Parsons, M. 2009. A comparison of single beam and multibeam sonar systems in seafloor habitat mapping. In: P*roc. 3rd Int. Conf. and Exhibition of Underwater Acoustic Measurements: Technologies & Results, Nafplion*, Greece (pp. 155-162).

Pickrill, R. A., & Todd, B. J. 2003. The multiple roles of acoustic mapping in integrated ocean management, Canadian Atlantic continental margin. *Ocean & Coastal Management*, 46(6-7), 601-614.

Rofallski, R., Tholen, C., Helmholz, P., Parnum, I., & Luhmann, T. 2020. Measuring artificial reefs using a multi-camera system for unmanned underwater vehicles. *International Archives of the Photogrammetry, Remote Sensing and Spatial Information Sciences-ISPRS Archives,* 43(B2), 999-1008.

Shortis, M,. 2019. Camera calibration techniques for accurate measurement underwater. *3D recording and interpretation for maritime archaeology*, 11-27.

Takasu, T. 2013. RTKLIB ver. 2.4. 2 Manual. RTKLIB: An Open Source Program Package for GNSS Positioning, 29, 49.